

Supporting Information

Transition metal electrocatalysts encapsulated into N-doped carbon nanotubes on reduced graphene oxide nanosheets: Efficient water splitting through synergistic effects

*Wenchao Wan, Shiqian Wei, Jingguo Li, Carlos A. Triana, Ying Zhou and Greta R. Patzke**

W. Wan, J. Li, Dr. C. A. Triana, Prof. G. R. Patzke

Department of Chemistry, University of Zurich, Winterthurerstrasse 190, CH-8057 Zurich, Switzerland.

E-mail: greta.patzke@chem.uzh.ch

S. Wei, Prof. Y. Zhou

The Center of New Energy Materials and Technology, School of Materials Science and Engineering, Southwest Petroleum University, Chengdu 610500, China

Table of Contents

<u>I. Experimental section, methods and computational details</u>	4
<u>II. Structural characterization, performance and DFT</u>	
Table S1. Results of Bader charge population analyses.	9
Table S2. Zero-point energy corrections and entropic contributions to free energies.	9
Table S3. Change of the free energy in ΔZPE and ΔS .	10
Table S4. Change of the free energy in each step over three different models.	10
Table S5. ΔE (H^*), ZPE (H^*), ΔZPE and ΔG (H^*) of H^* at the adsorption sites.	11
Table S6. Calculation of HER activation energy on the catalysts.	11
Figure S1. PXRD patterns of bare NiFe alloy, NiFe-N-CNT, and NiFe-N-CNT-rGO.	12
Figure S2. PXRD patterns of bare graphene and C_3N_4 -graphene.	12
Figure S3. Raman spectra and PXRD patterns of GO and rGO.	13

Figure S4. SEM and TEM images of NiFe-N-CNT.	13
Figure S5. Representative SEM image of bare NiFe alloy.	14
Figure S6. HRTEM image of NiFe-N-CNT-rGO.	14
Figure S7. SEM image of C ₃ N ₄ -graphene after thermal reduction at 900 °C.	15
Figure S8. SEM images of g-C ₃ N ₄ and NiFe-N-CNT catalysts.	15
Figure S9. TGA measurement of NiFe-N-CNT.	16
Figure S10. PXRD patterns and Raman spectra of C ₃ N ₄ -NiFe.	16
Figure S11. SEM images of CNT encapsulated Fe, Co, Ni, CoNi and CoFe.	17
Figure S12. Photographs of the precursors and final products.	17
Figure S13. Complete XPS spectra of NiFe-N-CNT and NiFe-N-CNT-rGO.	18
Table S7. XPS analyses of NiFe-N-CNT and NiFe-N-CNT-rGO.	18
Figure S14. High-resolution XPS spectra of NiFe-N-CNT.	19
Figure S15. EDX mapping of a representative NiFe-N-CNT sample.	19
Figure S16. Electrocatalytic water splitting activities of NiFe-N-CNT-rGO.	20
Figure S17. Electrocatalytic water splitting activities of NiFe-N-CNT-rGO.	20
Figure S18. OER and HER activities normalized to the catalyst mass.	21
Figure S19. Comparison of activities to NiFe NPs without incorporation into CNTs.	21
Figure S20. Overall water splitting measurement.	22
Table S8. BET surface areas.	22
Table S9. ICP-MS measurement of NiFe-N-CNT and NiFe-N-CNT-rGO.	22
Figure S21. Long-term chronoamperometric test on Ni foam.	23
Figure S22. TEM and SEM images of NiFe-N-CNT-rGO after OER.	24
Figure S23. TEM and SEM images of NiFe-N-CNT after HER.	24
Figure S24. Fe K-edge XANES spectra of NiFe-N-CNT-rGO before and after OER.	25
Figure S25. Ni K-edge XANES spectra of NiFe-N-CNT-rGO before and after OER.	25

Figure S26. Nitrogen adsorption-desorption isotherms.	26
Figure S27. Calculated models for the adsorption of the intermediates.	27
Figure S28. Free energy profiles for the OER.	28
Figure S29. Calculated charge densities and surface electronic structures.	29
Table S10. Elemental analysis data for NiFe-N-CNT samples.	30
Table S11. Activity comparison with previous literature.	31
<u>III. References</u>	32

Experimental section

Materials: Dicyandiamide ($C_2H_4N_4$) (>99 %), was purchased from Alfa Aesar. All other metal salts ($Ni(NO_3)_2 \cdot 6H_2O$ (≥ 98.0 %), $Co(NO_3)_2 \cdot 6H_2O$ (≥ 98.0 %), $Fe(NO_3)_2 \cdot 6H_2O$ (≥ 98.0 %)) were purchased from Sigma-Aldrich. Graphite powder (average lateral size of 20 μm), $KMnO_4$, H_2O_2 (30 %), $K_2S_2O_8$, and P_2O_5 (≥ 98.0 %) were purchased from Sigma-Aldrich. Sulfuric acid (98 %) and nitric acid (65 %) were purchased from Merck KGaA, Germany. N_2 gas used in the synthesis was purchased from PanGas AG, Switzerland, ≥ 99.9999 %.

Materials synthesis:

Graphite phase carbon nitride (g- C_3N_4) was obtained from a thermopolymerization procedure, in which $C_2H_4N_4$ was put into a crucible (with lip) and heated at 550 °C for 2 h under air atmosphere with a ramp rate of about 2.3 °C/min. The obtained yellow bulk g- C_3N_4 was then ground into a powder with a mortar for further use.

Graphene oxide (GO) was prepared via a modified Hummer method.¹ First, commercial graphite flakes (5 g), 98% sulfuric acid (150 mL) and fuming nitric acid (50 mL) were stepwise added into a flask with continuous stirring at room temperature for 24 h. Then the mixture was poured into water and collected by filtration. After the filtration step, the collected solid was repeatedly washed with water and completely dried in the oven at 60 °C. The dried graphite powder was thermally expanded at 1000 °C for 30 s to obtain expanded graphite. 4.2 g $K_2S_2O_8$ and 6.2 g P_2O_5 were added into 300 mL sulfuric acid within a 500 mL flask and the mixture was kept at 90 °C for complete dissolution of $K_2S_2O_8$ and P_2O_5 . After cooling down to 80 °C, the EG powder was successively added into the above solution at 80 °C for 5 h. After cooling down to room temperature, the mixture was diluted into water and collected by centrifugation, washed with water several times, and finally dried in an oven at 60 °C. The dried expanded graphite was pulverized and thermally expanded at 1000 °C for 30 s again. After the expanding procedure, 1 g graphite was added into 50 mL concentrated H_2SO_4 (0 °C), and then 6 g $KMnO_4$ was added slowly under continuous stirring (under 15 °C) for 2 h. Then the mixture was heated up to 35 °C and stirred for 2 h. The mixture was finally diluted with 2 L water, followed by dropwise adding 10 mL 30 % H_2O_2 . The mixture was left undisturbed for 2 d and the nearly clear supernatant was then decanted. The precipitate was repeatedly washed by centrifugation (10000 rpm) with water, 1 M HCl solution and water successively. After the GO solution was neutral, centrifugation washing with 2000 rpm was conducted to collect the supernatant liquid.

NiFe-N-CNTs were synthesized via a thermal reduction protocol. 10 mg $\text{Ni}(\text{NO}_3)_2 \cdot 6\text{H}_2\text{O}$ and 10 mg $\text{Fe}(\text{NO}_3)_3 \cdot 9\text{H}_2\text{O}$ were first mixed with 500 mg g- C_3N_4 powder in deionized water. After 1 h ultrasonic and 24 h stirring treatment, the mixture was further subjected to a freeze-drying procedure to achieve a metal adsorbed g- C_3N_4 powder. The above powder was subsequently treated with a thermal reduction step in a tube furnace at temperatures from 500 to 1100 °C under protective N_2 atmosphere. For different mass ratios of metal or alloy, the mass of g- C_3N_4 was fixed at 500 mg, and metal salts were applied with the corresponding weight. To obtain different ratios of the metals in the hybrid alloy-CNT catalysts, the total mass of the metal salts was fixed at 20 mg by adjusting the molar ratio of the metals. Other metals and alloys encapsulated N-CNT were fabricated via the same protocol with the exception of adding different metal salts.

Metal and alloy-CNT-rGO were synthesized by adding 15 mL GO solution (0.8 mg/mL) into the mixture after the ultrasonic process, while the other steps were performed as described for the preparation of metal and alloy-CNT.

Sample preparation for electrochemical characterization: 2.5 mg of catalyst was dispersed in 0.5 mL of water and 0.5 mL of ethanol. After 30 min ultrasonic treatment, 50 μL of 5 wt % Nafion solution was further added into the above solution with another 60 min sonication to form a homogeneous ink. Then 5 μL of the catalyst ink (containing 12.5 μg of catalyst) was loaded onto a glassy-carbon electrode (2 mm in diameter).

Electrochemical measurements: Electrochemical measurements were carried out on a PalmSens3 electrochemistry workstation with the standard three-electrode system in 1 M KOH electrolyte. Glassy carbon (GC) electrode loaded with catalyst was used as working electrode. Ag/AgCl with saturated KCl filling solution and platinum wire were used as reference electrode and counter electrode, respectively. The catalyst electrodes were continuously scanned by CV until a stable CV curve could be repeated before measuring polarization curves. The scan rates for all the LSV and CV measurements were set to 10 mV/s to minimize the capacitive current. Electrochemical impedance spectroscopy (EIS) studies were performed when the working electrode was biased at certain potentials while sweeping the frequency from 10 kHz to 10 mHz with a 5 mV ac amplitude.

Materials characterization:

Powder X-ray diffraction (PXRD) patterns were recorded on a STOE STADI P diffractometer (transmission mode, Ge monochromator) with Mo K_{α} radiation. Raman spectra were measured with a Renishaw Ramascope as pristine powder samples on quartz glass slides. Scanning electron microscope (SEM) images were recorded on a Zeiss SUPRA 50VP SEM. Transmission electron microscopy (TEM) images were recorded with a FEI Tecnai G2 F20 microscope operated at 200 kV equipped with an Oxford EDX system. X-ray photoelectron spectroscopy (XPS) measurements were conducted on a Thermo ESCALAB 250Xi. Elemental analysis was performed at Mikroanalytisches Labor Pascher (Remagen/Germany). Inductively coupled plasma mass spectrometry (ICP-MS) measurements were carried out on an Agilent 8800 instrument. All the samples were first annealed under air atmosphere, and then dissolved in aqua regia. Thermogravimetric analysis (TGA) of the samples was conducted using a Netzsch Jupiter STA 449 F3 TGA within the temperature range from 25 °C to 800 °C and with a heating rate of 10 °C/ min under N_2 atmosphere. Nitrogen sorption isotherms were recorded after degassing at 100 °C overnight under vacuum with a Quantachrome Quadasorb SI porosimeter.

X-ray absorption spectroscopy (XAS). X-ray-absorption near-edge structure (XANES) and extended X-ray-absorption fine structure (EXAFS) experiments at the Ni and Fe K -edges on solid samples dispersed in cellulose of pristine and post-catalytic NiFe-N-CNT-rGO and those of reference oxides NiO, FeO and Fe_2O_3 were carried out at the European Synchrotron Radiation Facility (ESRF), Swiss-Norwegian Beamline BM31, Grenoble, France. The storage ring was run in top-up mode with an average current of 400 mA. The X-ray beam was collimated using a Si coated mirror and the energy was scanned using a channel-cut Si[111] monochromator. Measurements were done at room temperature using a three-ionization chamber configuration in transmission mode using a 13-element Ge detector. For energy calibration spectra of metal Ni and Fe foils were also measured. The measured EXAFS spectra $k^2\chi(k)$ were extracted by standard data reduction, absorption edge energy calibration and background subtraction as implemented in ATHENA.² The spectra were reduced into the range $\Delta k \approx 3-12 \text{ \AA}^{-1}$ and Fourier-Transformed to $FT|k^2\chi(k)|$ into the real-space interval $\Delta R \approx 0-6 \text{ \AA}$. To calculate main values for interatomic distances, coordination numbers and Debye-Waller factors (σ^2), nonlinear least-squares fitting of the $FT|k^2\chi(k)|$ spectra was done by ARTEMIS² using atomic clusters of NiFe generated by ATOMS² as implemented in IFEFFIT.² Amplitudes and phase shifts for single and multiple scattering paths were calculated using the FEFF6 code.³

Density functional theory (DFT) calculations

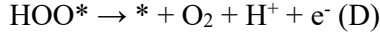
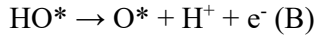
All DFT calculations were performed using the Vienna Ab Initio Simulation Package (VASP) with a cut-off energy of 400 eV. The generalized gradient approximation of the Perdew-Burke-Ernzerhof (PBE) functional was used for the exchange-correlation function. An icosahedral Ni₈Fe₅ metal cluster which was applied in previous work^{4,5} was wrapped into a carbon tube consisting of 112 carbon atoms to construct the calculation model. The periodic models were fully relaxed to the ground state, and the convergence criteria of energy and force were 1×10^{-4} eV and 0.05 eV/Å for the structure relaxations, respectively. The van der Waals interactions in the systems were described by the DFT-D2 method of Grimme.

Hydrogen Evolution Reaction (HER)

It is well known that the hydrogen evolution reaction (HER) activity over a given system can be closely correlated to the adsorption energy of a single H atom on the system. Thus, the free energy of H* (ΔG (H*)) is usually considered as an effective descriptor for evaluating the HER activity of the system. Generally, the smaller the ΔG (H*) absolute value, the better the HER activity of the system.⁵ The free energies of the studied systems can be computed by the formula ΔG (H*) = ΔE (H) + ΔZPE - $T\Delta S$, where ΔE (H*), ΔZPE and ΔS are the binding energy, zero-point energy change and entropy change of H* adsorption, respectively. In this work, ΔE (H) was calculated by $\Delta E(H) = E(H^*) - E(^*) - 1/2 E_{H_2}$, ΔS was calculated by using the equation $\Delta S = S(H^*) - 1/2S(H_2) \approx -1/2S(H_2)$, because of the negligible vibrational entropy of H*. Considering that $TS(H_2)$ is 0.40 eV for H₂ at 298 K and 1 atm, the corresponding $T\Delta S$ was determined to be -0.20 eV. Additionally, the equation $\Delta ZPE = ZPE(H^*) - 1/2ZPE(H_2)$ was used to estimate ΔZPE for H*. It is noteworthy that our computed value for $ZPE(H_2)$ was about 0.294 eV, which is close to a previous report.⁶

Oxygen Evolution Reaction (OER)

Of the two half reactions involved in the water-splitting reaction (*i.e.*, the HER and OER), OER is more complex due to the four electron transfer process involved. Usually, the scheme developed by Nørskov *et al.*⁷ can be employed to gain an insight into the OER, where the OER is assumed to involve four elementary reaction steps and each step involves electron transfer accompanied by proton release, as indicated below:



where $*$ and X^* represent an adsorption site and an adsorbed X intermediate on the surface, respectively. The free energy of $\text{H}^+ + \text{e}^-$ can be half of the formation energy of H_2 at 298 K and 1 atm. The free energy of the OER is computed by the equation $\Delta G = \Delta E + \Delta \text{ZPE} - T\Delta S$. The value of ΔE was obtained from computation of geometrical structures. The values of ΔZPE and ΔS were determined by employing the computed vibrational frequencies and standard tables for the reactants and products in the gas phase. The entropy for the adsorbed atoms/molecules at the surface of active site was assumed to be zero. The temperature dependence of the enthalpy was neglected in the calculations. Moreover, an external bias U was imposed on each step by including a $-eU$ term in the computation of reaction free energy. Consequently, the reaction free energy of each step could be expressed as follows:

$$\Delta G_A = E(\text{HO}^*) - E(*) - E_{\text{H}_2\text{O}} + 1/2E_{\text{H}_2} + (\Delta \text{ZPE} - T\Delta S)_A - eU \text{ (1)}$$

$$\Delta G_B = E(\text{O}^*) - E(\text{HO}^*) + 1/2E_{\text{H}_2} + (\Delta \text{ZPE} - T\Delta S)_B - eU \text{ (2)}$$

$$\Delta G_C = E(\text{HOO}^*) - E(\text{O}^*) - E_{\text{H}_2\text{O}} + 1/2E_{\text{H}_2} + (\Delta \text{ZPE} - T\Delta S)_C - eU \text{ (3)}$$

$$\Delta G_D = E(*) - E(\text{HOO}^*) + E_{\text{O}_2} + 1/2E_{\text{H}_2} + (\Delta \text{ZPE} - T\Delta S)_D - eU \text{ (4)}$$

where $E(*)$, $E(\text{HO}^*)$, $E(\text{O}^*)$, and $E(\text{HOO}^*)$ are the computed DFT energies of the pure surface and the adsorbed surfaces with HO^* , O^* , and HOO^* , respectively. $E_{\text{H}_2\text{O}}$, E_{H_2} and E_{O_2} are the computed energies for the sole H_2O , H_2 and O_2 molecules, respectively. For the total reaction $\text{H}_2\text{O} \rightarrow 1/2\text{O}_2 + \text{H}_2$, the free energy change was fixed at the experimental value of 2.46 eV per water molecule.⁷ When forming one molecule of O_2 in the reaction step, the reaction free energy can be expressed as $\Delta G_{(2\text{H}_2\text{O} \rightarrow \text{O}_2 + 2\text{H}_2)} = 4.92 \text{ eV} = E_{\text{O}_2} + 2E_{\text{H}_2} - 2E_{\text{H}_2\text{O}} + (\Delta \text{ZPE} - T\Delta S)_{(2\text{H}_2\text{O} \rightarrow \text{O}_2 + 2\text{H}_2)}$. The reaction overpotential could be obtained by evaluating the difference between the minimum voltage needed for the OER and the corresponding voltage needed for changing all the free-energy steps into downhill.⁶

Table S1. Amount of transferred electrons from metal to graphene (Δq) based on Bader charge population analyses.

Models	NiFe-CNT	NiFe-N-CNT
Δq (e)	1.54	1.60

Table S2. Zero-point energy corrections and entropic contributions to free energies.

	TS	ZPE			
		CNT	NiFe-CNT	NiFe-N-CNT	NiFe
H₂O	0.67	0.57	0.57	0.57	0.57
O₂	0.64	0.10	0.10	0.10	0.10
H₂	0.41	0.27	0.27	0.27	0.27
HO*	0	0.38	0.39	0.38	0.31
O*	0	0.09	0.08	0.10	0.07
HOO*	0	0.45	0.45	0.46	0.41
H*	0	0.30	0.31	0.32	0.15

Table S3. Change of the free energy arising from the differences in zero-point energies, ΔZPE , and the change in entropy ΔS for the different reaction steps.

	$\text{H}_2\text{O} + * \rightarrow \text{HO}^* + \frac{1}{2} \text{H}_2$	$\text{HO}^* \rightarrow \text{O}^* + \frac{1}{2} \text{H}_2$	$\text{H}_2\text{O} + \text{O}^* \rightarrow \text{HOO}^* + \frac{1}{2} \text{H}_2$	$\text{HOO}^* \rightarrow \text{O}_2 + * + \frac{1}{2} \text{H}_2$
	$(\Delta ZPE - T\Delta S)_A$	$(\Delta ZPE - T\Delta S)_B$	$(\Delta ZPE - T\Delta S)_C$	$(\Delta ZPE - T\Delta S)_D$
CNT	0.42	-0.34	0.39	-0.47
NiFe-CNT	0.43	-0.36	0.41	-0.48
NiFe-N-CNT	0.45	-0.34	0.40	-0.51
NiFe	0.36	-0.31	0.37	-0.42

Table S4. Change of the free energy in each step over three different models.

	$\Delta G_A/\text{eV}$	$\Delta G_B/\text{eV}$	$\Delta G_C/\text{eV}$	$\Delta G_D/\text{eV}$
CNT	2.36	0.78	2.56	-0.78
NiFe-CNT	1.23	1.04	2.31	0.34
NiFe-N-CNT	0.35	1.36	2.30	0.91
NiFe	-0.825	0.11	3.96	1.67

Table S5. Values of ΔE (H*), ZPE (H*), ΔZPE and ΔG (H*) of the H* at the adsorption sites.

	$\Delta E(\text{H}^*)/\text{eV}$	$ZPE(\text{H}^*)/\text{eV}$	$\Delta ZPE(\text{H}^*)/\text{eV}$	$T\Delta S$	$\Delta G(\text{H}^*)/\text{eV}$
CNT	-2.3	0.30	0.166	-0.20	1.5
NiFe-CNT	-0.065	0.30	0.17	-0.20	0.3
NiFe-N-CNT	-0.62	0.32	0.19	-0.20	-0.2
NiFe	-0.74	0.152	0.016	-0.20	-0.524

Table S6. Calculation of HER activation energy on the catalysts.

	$\Delta E(\text{H}_2\text{O})/\text{eV}$	$\Delta E(\text{OH})/\text{eV}$	$\Delta E(\text{H})/\text{eV}$
NiFe	-0.79	-0.825	-0.524
NiFe-CNT	-0.52	1.23	0.3
NiFe-N-CNT	-0.13	0.35	-0.2
CNT	0.81	2.36	1.5

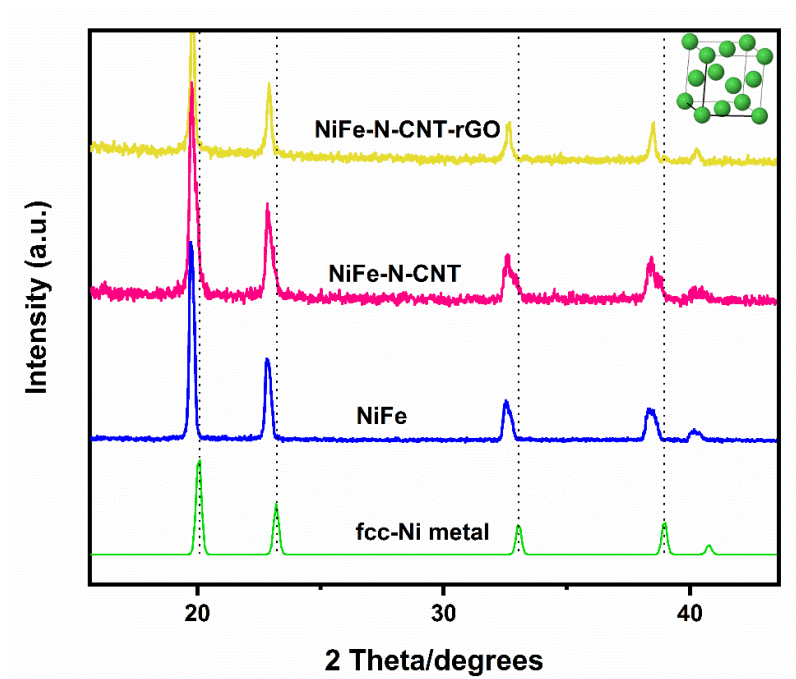


Figure S1. PXRD patterns of bare NiFe alloy, NiFe-N-CNT, and NiFe-N-CNT-rGO vs. Ni metal reference.

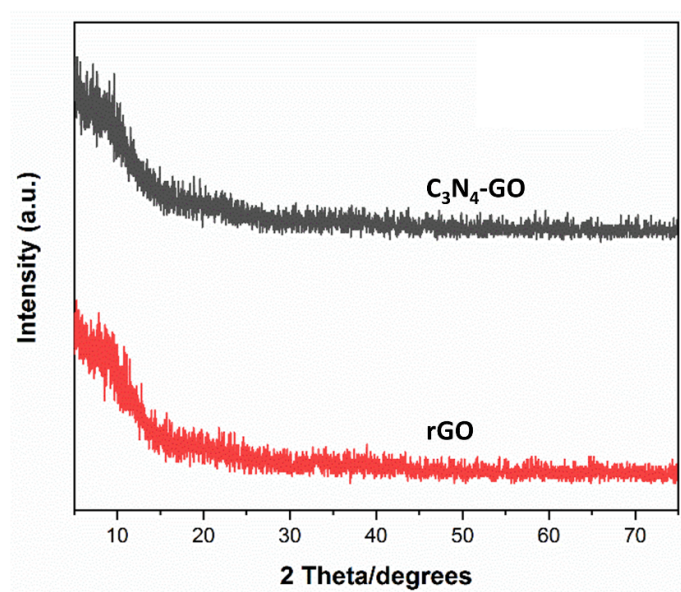


Figure S2. PXRD patterns of bare rGO and C₃N₄-GO on Mo tube.

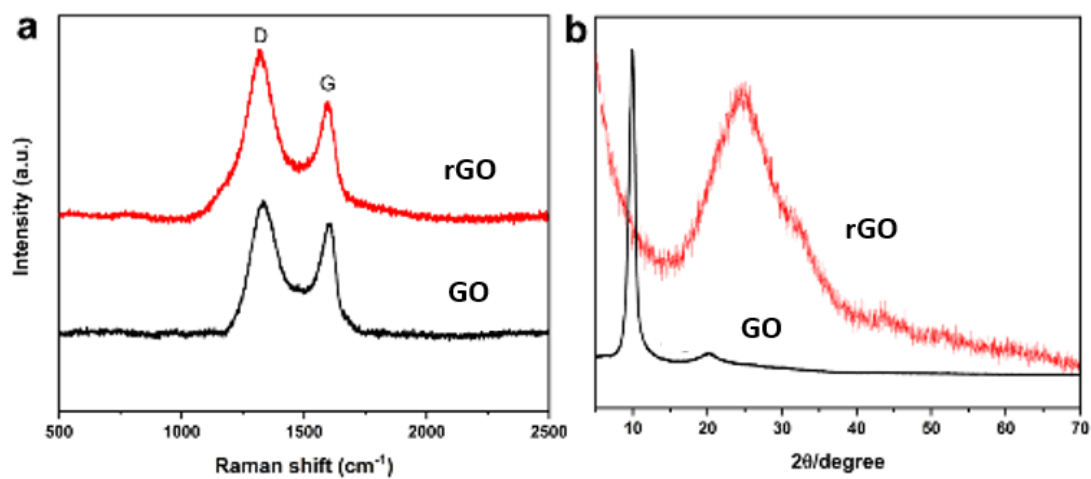


Figure S3. Raman spectra and PXRD patterns (CuK_α radiation) of initial GO and rGO after pyrolysis at 800°C.

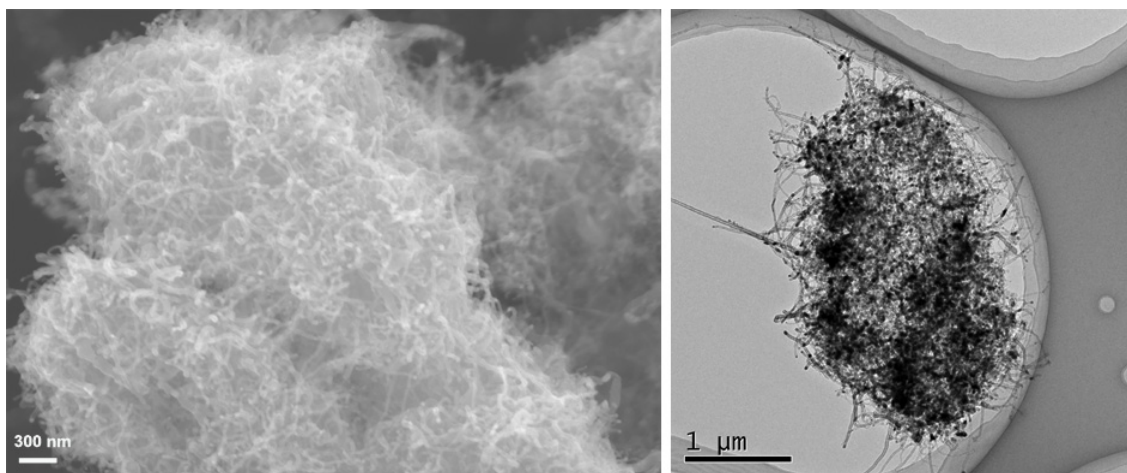


Figure S4. SEM and TEM images of NiFe-N-CNT.

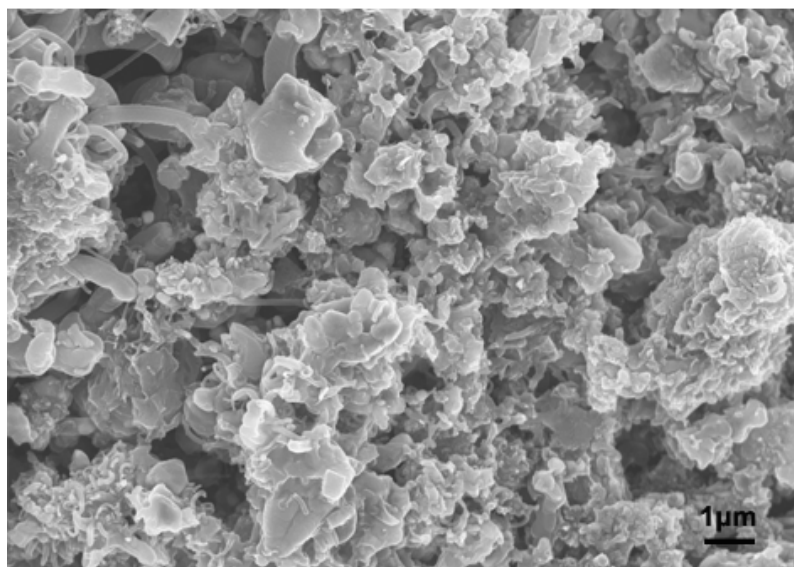


Figure S5. Representative SEM image of bare NiFe alloy.

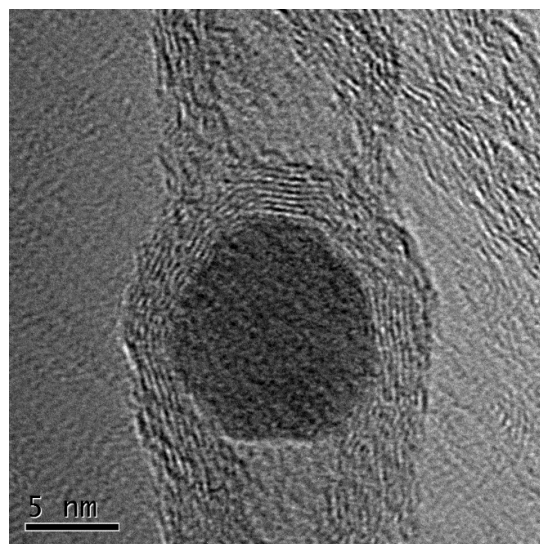


Figure S6. HRTEM image of NiFe-N-CNT-rGO.

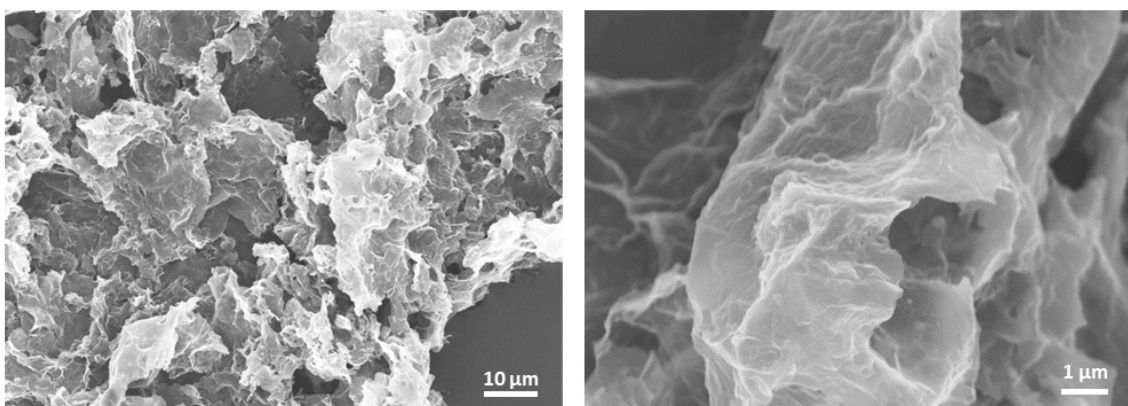


Figure S7. SEM images of C₃N₄-graphene after thermal reduction at 900 °C.

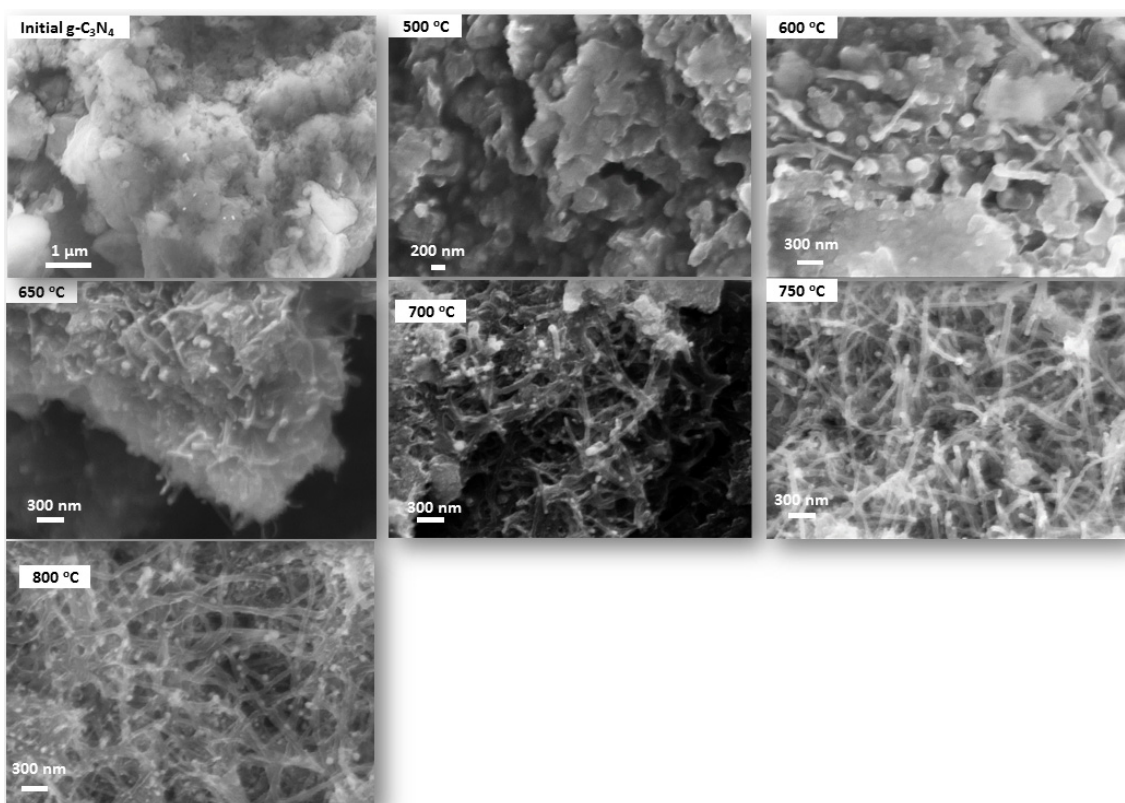


Figure S8. SEM images of g-C₃N₄ and NiFe-N-CNT catalysts prepared at different temperatures from 500 °C to 800 °C.

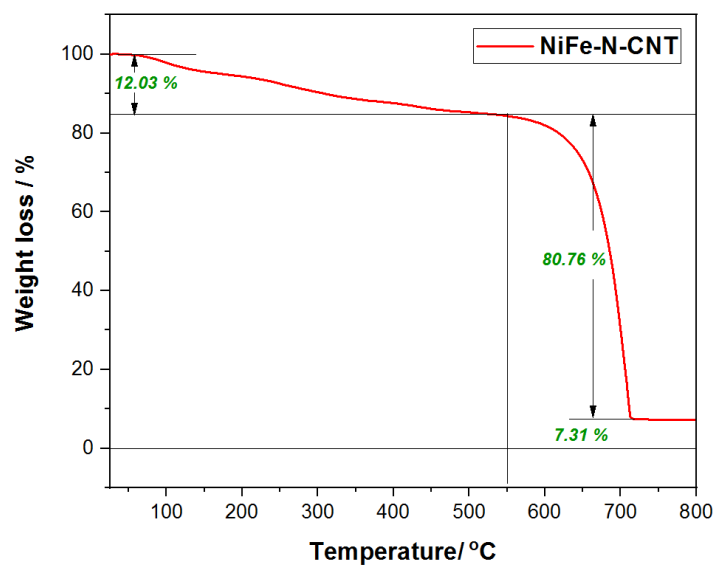


Figure S9. TGA measurement of NiFe-N-CNT.

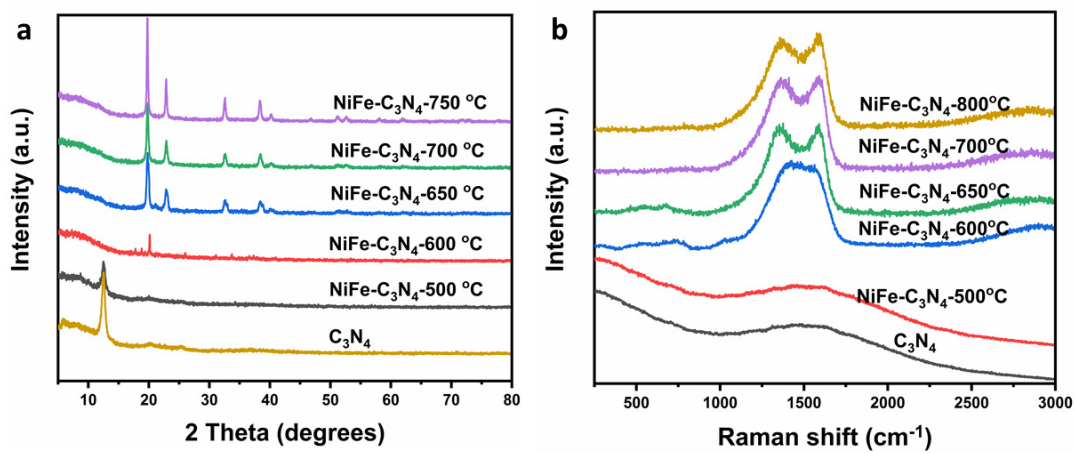


Figure S10. (a) XRD patterns of C₃N₄-NiFe compounds prepared at different temperatures; (b) Raman spectra of C₃N₄-NiFe compounds prepared at different temperatures.

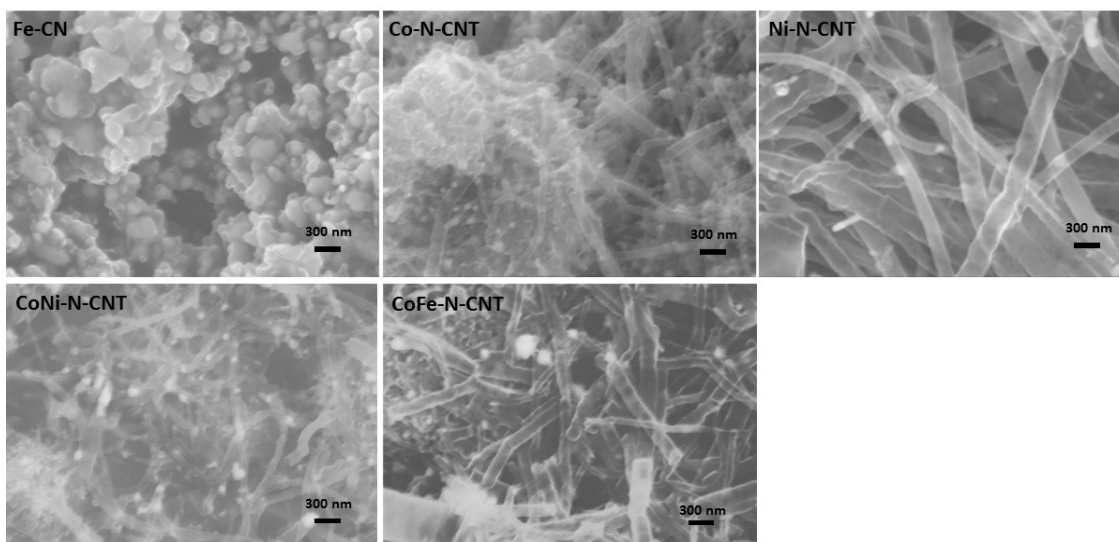


Figure S11. SEM images of CNT encapsulated Fe, Co, Ni, CoNi and CoFe (scale bar = 300 nm).

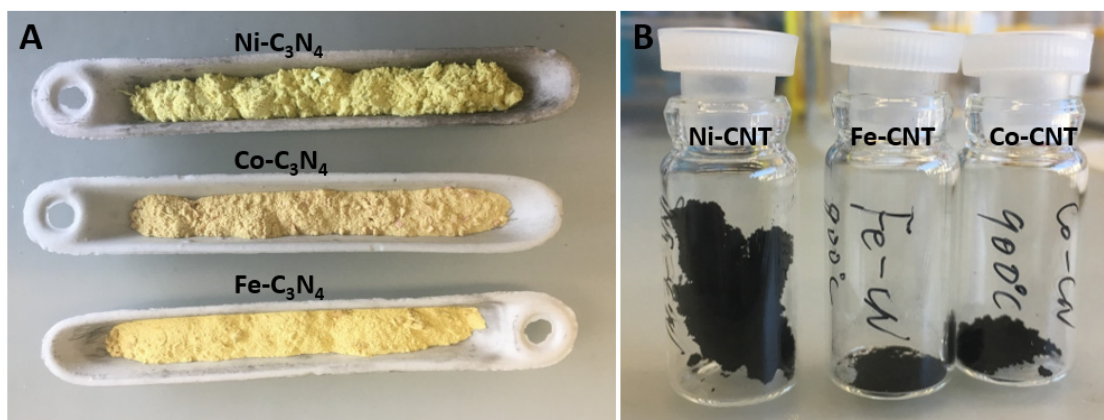


Figure S12. (a) Photographs of Ni, Co and Fe mixed with g-C₃N₄ after freeze drying; (b) final products after thermal reduction at 900 °C with the same amount of starting materials.

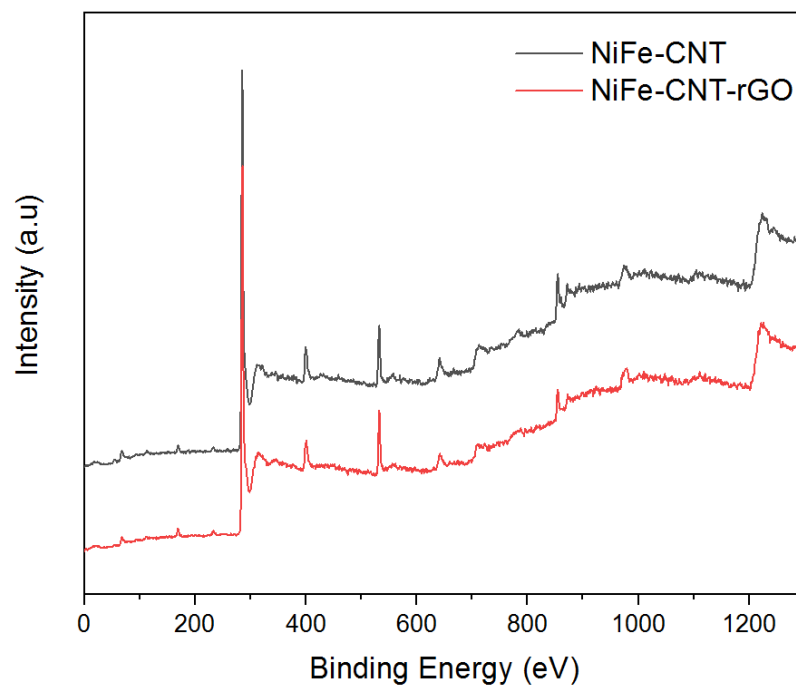


Figure S13. Complete XPS spectra of NiFe-N-CNT and NiFe-N-CNT-rGO.

Table S7. Atomic ratio of NiFe-N-CNT and NiFe-N-CNT-rGO determined from XPS fitting.

	C	N	Ni	Fe
NiFe-N-CNT	93.4 at%	5.7 at%	0.6 at%	0.3 at%
NiFe-N-CNT-rGO	94.2 at%	5.1 at%	0.4 at%	0.3 at%

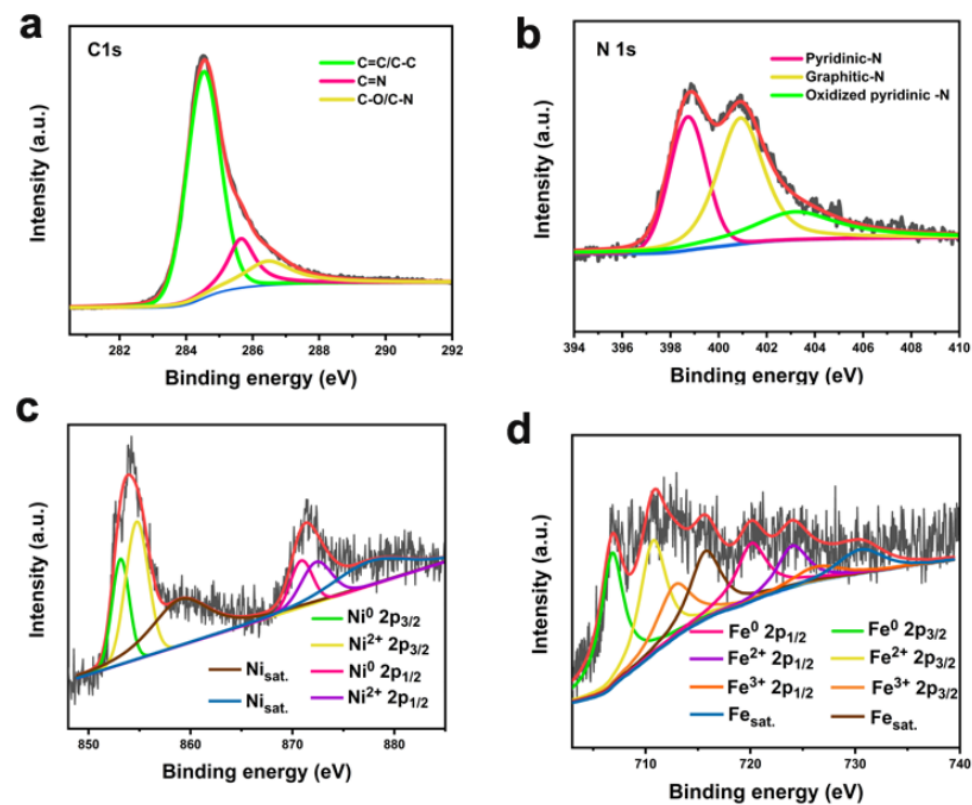


Figure S14. High-resolution XPS spectra of NiFe-N-CNT for the different elements.

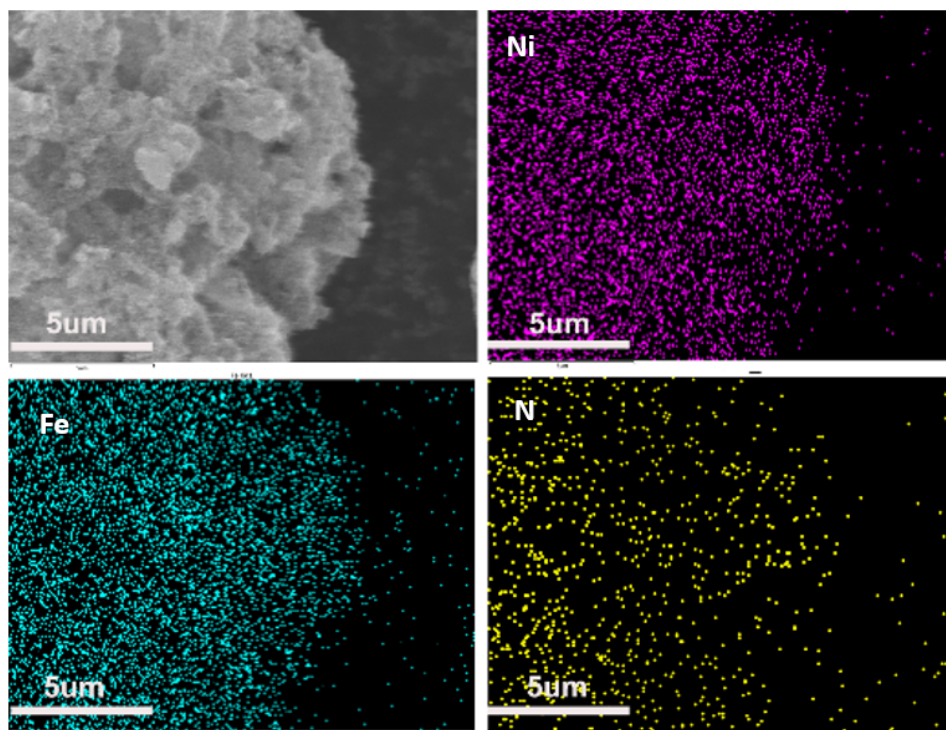


Figure S15. EDX mapping of a representative NiFe-N-CNT sample.

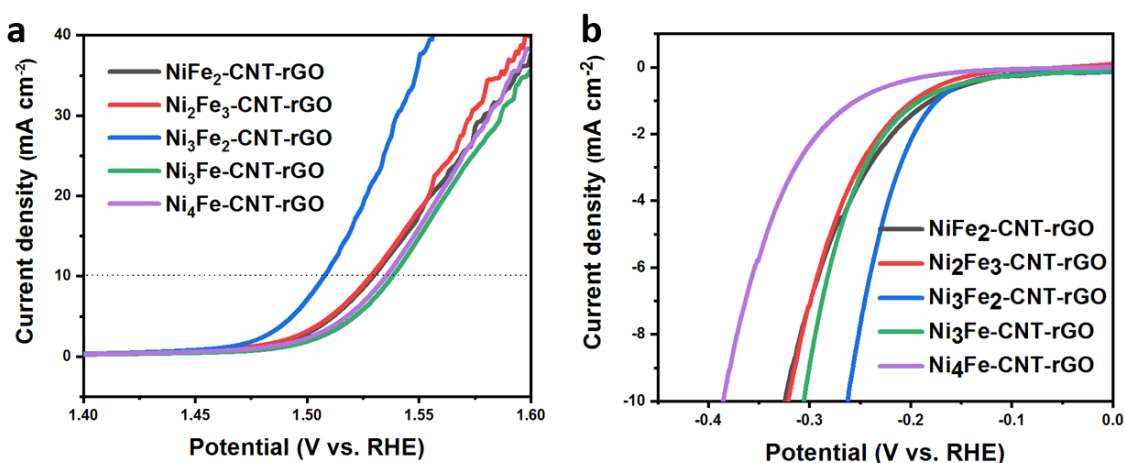


Figure S16. Electrocatalytic water-splitting activities of NiFe-N-CNT-rGO with different ratios of Ni/Fe. (a) LSV polarization curves for the OER, (b) LSV polarization curves for the HER.

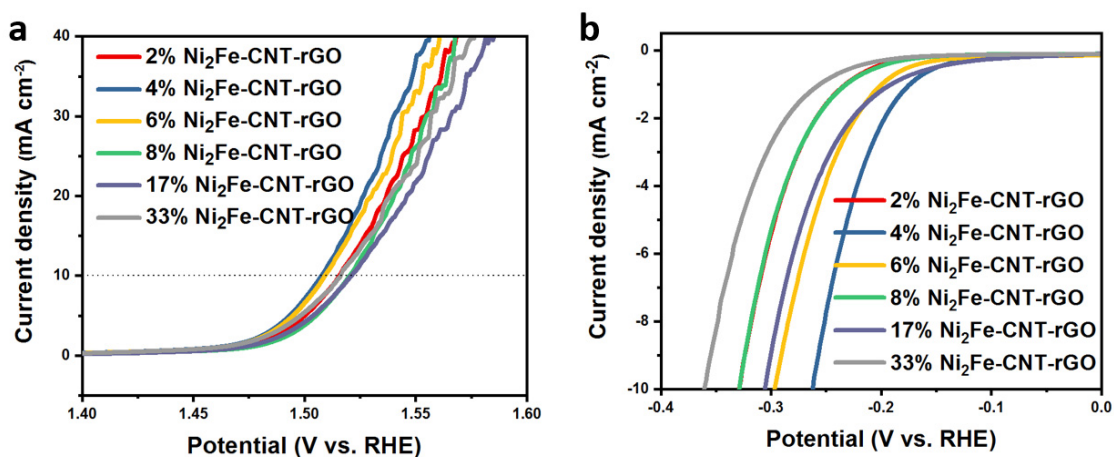


Figure S17. Electrocatalytic water-splitting activities of NiFe-N-CNT-rGO with different mass fractions of NiFe. (a) LSV polarization curves for the OER, (b) LSV polarization curves for the HER. (All ratios here are given as starting material compositions, for the sake of consistency with the main text.)

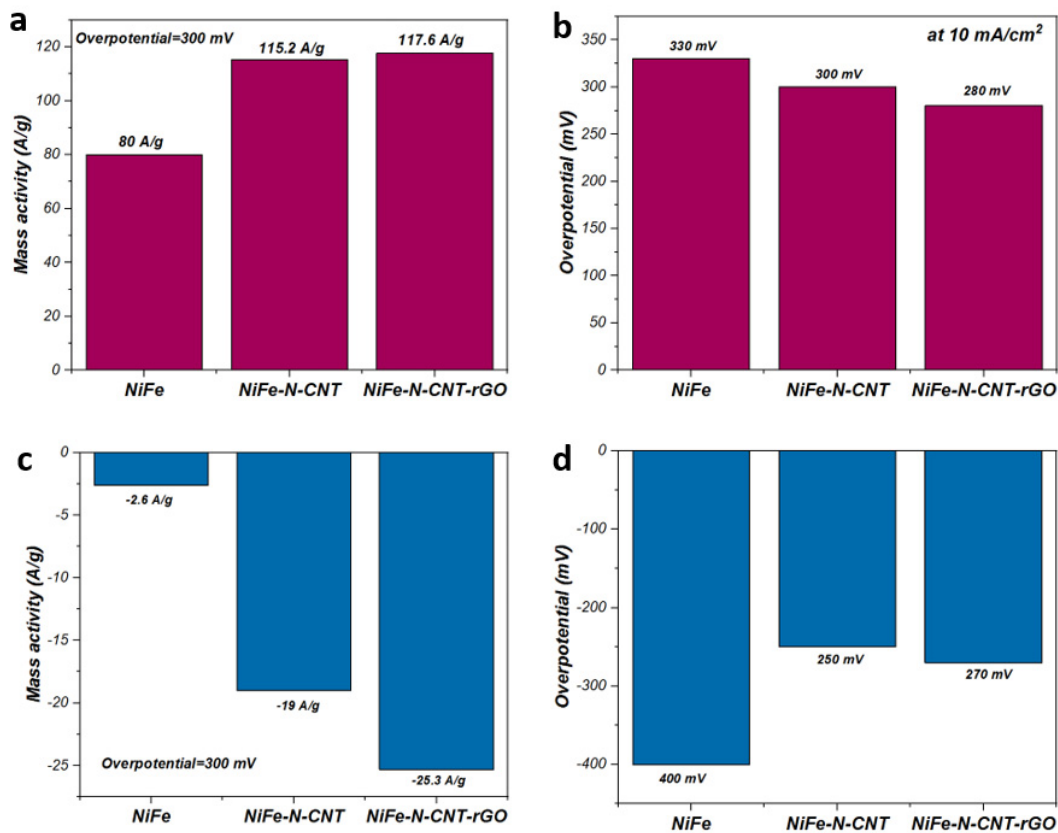


Figure S18. Corresponding OER and HER activities normalized to the catalyst mass (a,c) and to the electrochemical active area determined by double layer capacitance (b,d).

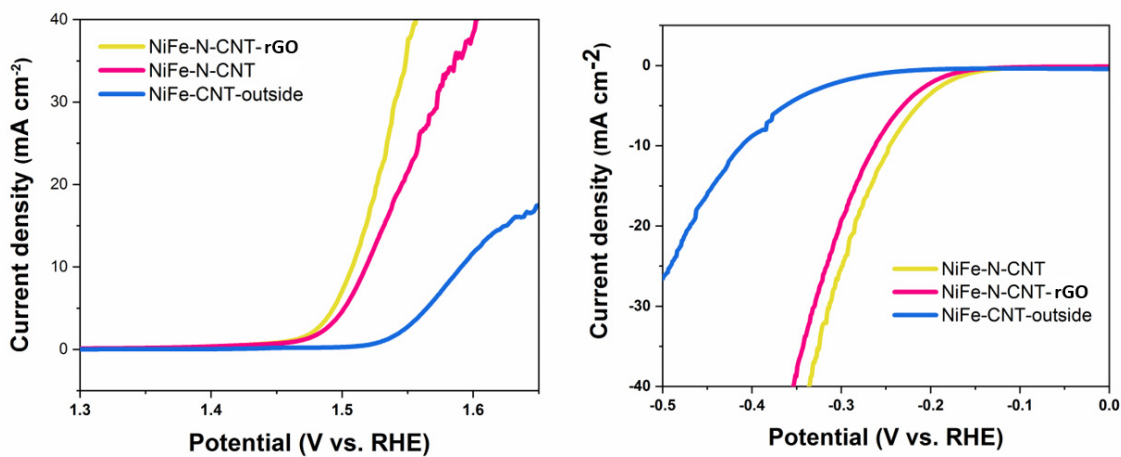


Figure S19. Comparison of OER and HER activities of NiFe-N-CNT and NiFe-N-CNT-rGO catalysts to NiFe NPs without incorporation into accompanying CNTs.

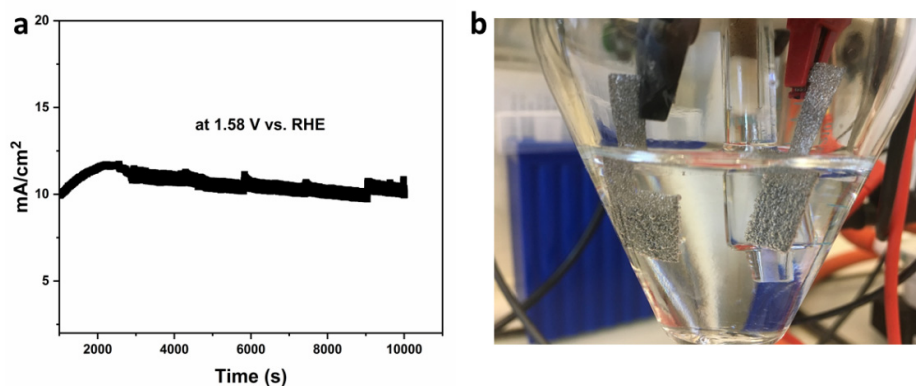


Figure S20 (a) Overall water splitting on Ni foam at potential of 1.58 V, (b) the photograph of the measurement.

Table S8. BET surface areas of NiFe, NiFe-N-CNT and NiFe-N-CNT-rGO.

	Specific surface area
NiFe	30 m ² /g
NiFe-N-CNT	129.9 m ² /g
NiFe-N-CNT-rGO	160.1 m ² /g

Table S9. ICP-MS measurement of NiFe-N-CNT and NiFe-N-CNT-rGO.

	First determination		Second determination		Average wt%
	(raw data)		(raw data)		(calculated)
	Fe [ng/ml]	Ni [ng/ml]	Fe [ng/ml]	Ni [ng/ml]	Total
NiFe-N-CNT-rGO	32.24	92.12	33.38	93.12	28.5%
NiFe-N-CNT	33.33	91.77	33.57	93.14	32.0%

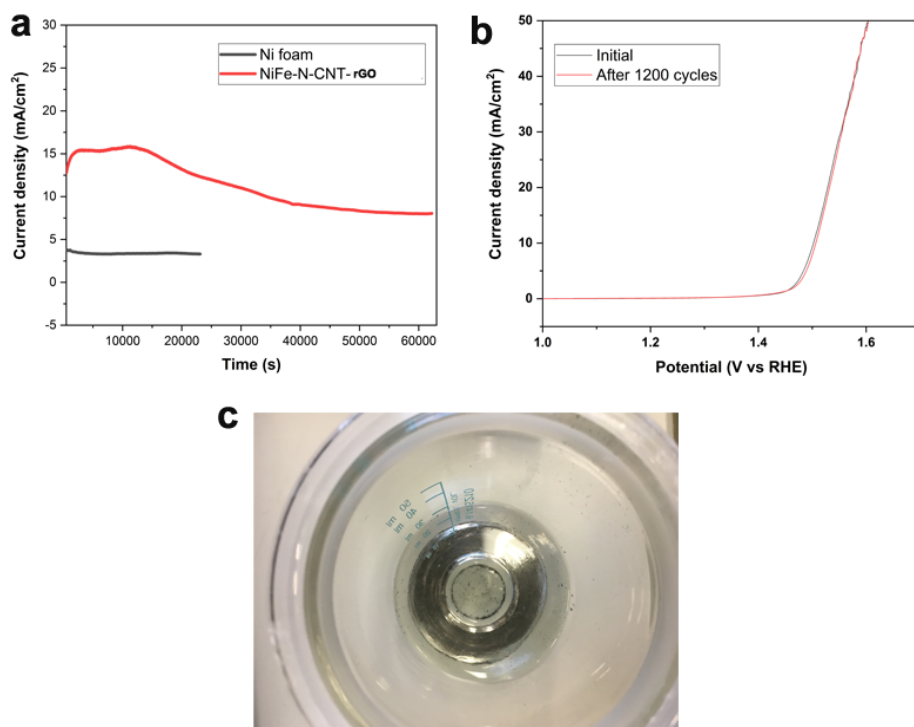


Figure S21. (a) Long-term chronoamperometric OER test of NiFe-N-CNT-rGO on Ni foam under the same overpotential compared to GC. (b) LSV curves before and after 1200 CV cycles. (c) Detachment of the catalyst suspended in the electrolyte after long-term measurement on Ni foam.

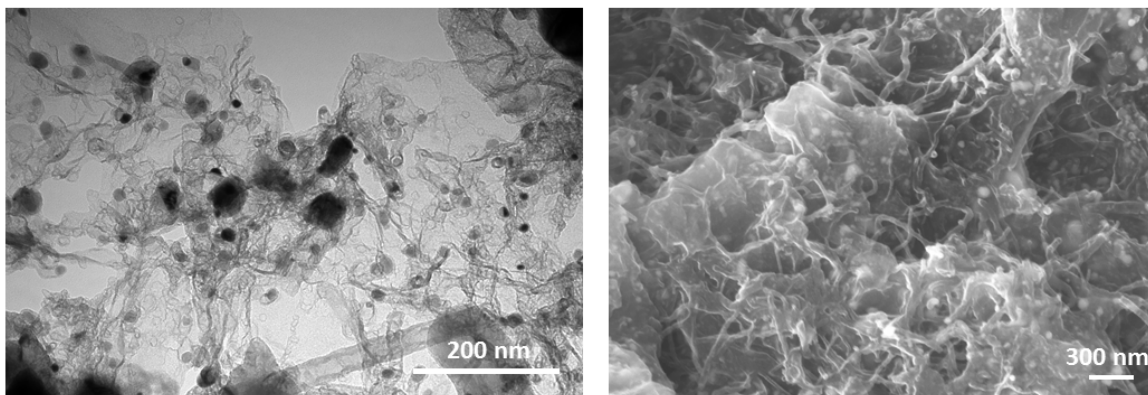


Figure S22. TEM (left) and SEM (right) images of NiFe-N-CNT-rGO after OER measurements.

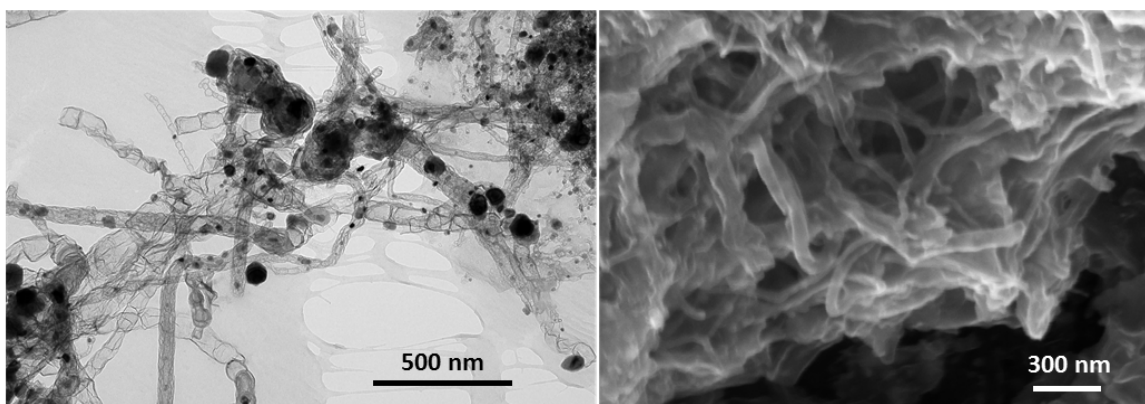


Figure S23. TEM (left) and SEM (right) images of NiFe-N-CNT after HER measurements.

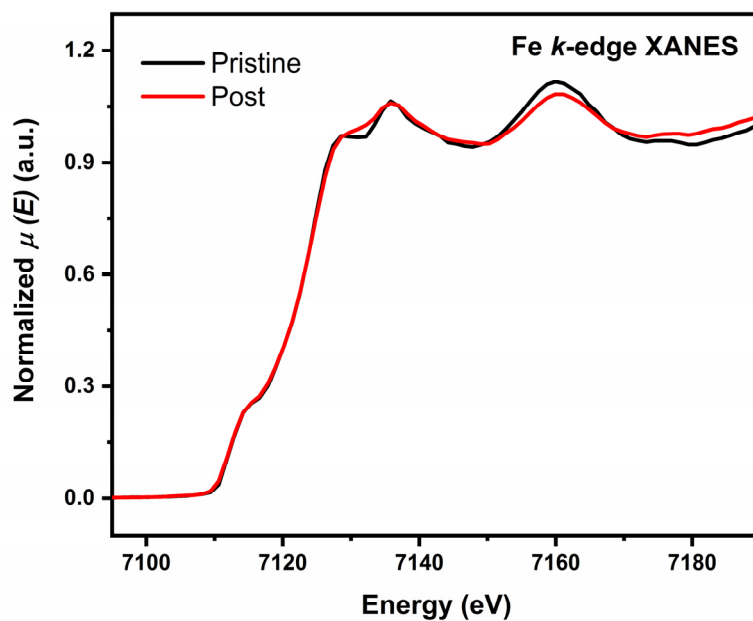


Figure S24. Fe K-edge XANES spectra of NiFe-N-CNT-rGO catalyst before and after OER.

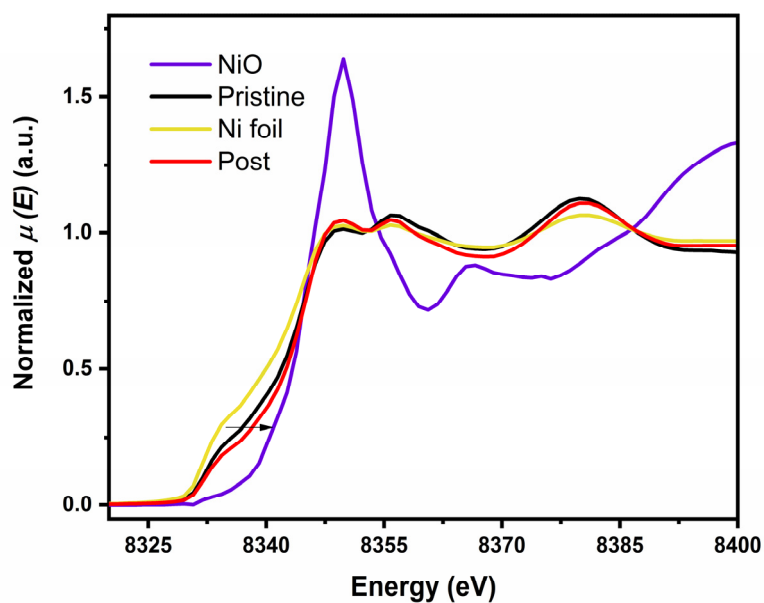


Figure S25. Ni K-edge XANES spectra of NiFe-N-CNT-rGO catalyst before and after electrocatalytic OER vs. reference samples.

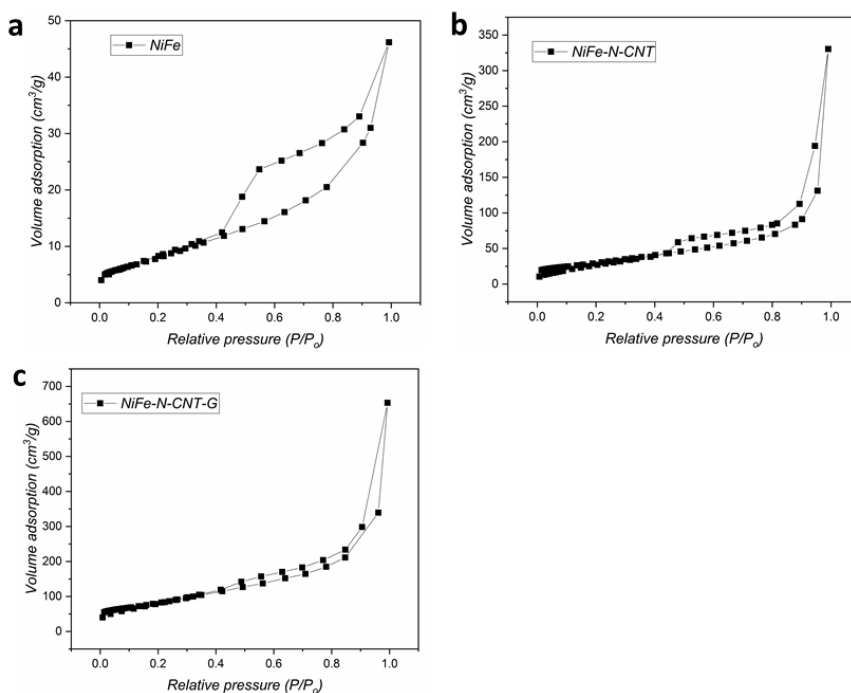


Figure S26. Nitrogen adsorption-desorption isotherms of NiFe, NiFe-N-CNT and NiFe-N-CNT-rGO.

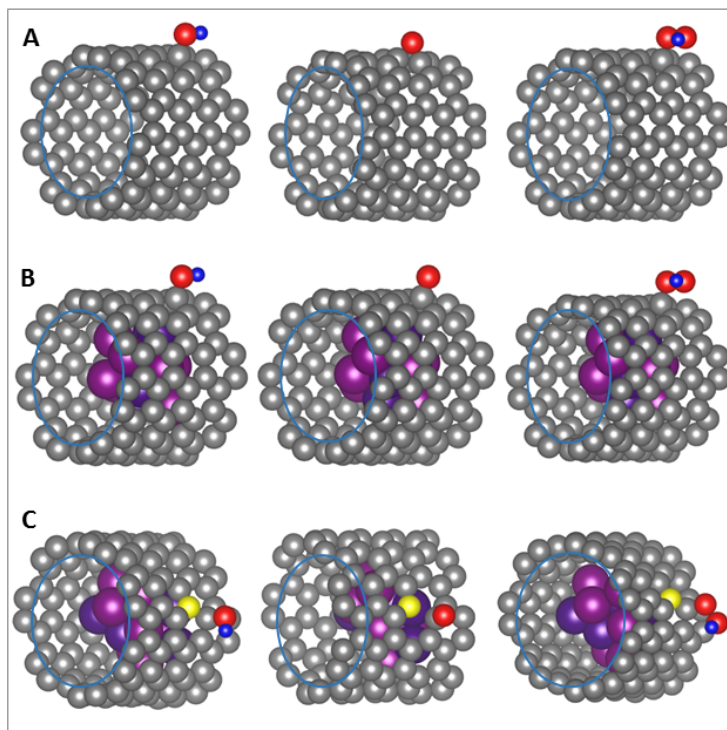


Figure S27. Calculated models for the intermediates adsorbed on (a) pure CNT, (b) CNT encapsulated NiFe alloy, (c) N-doped CNT encapsulated NiFe alloy (red, blue, gray, yellow, purple and deep purple spheres correspond to O, H, C, N, Ni, and Fe atoms, respectively).

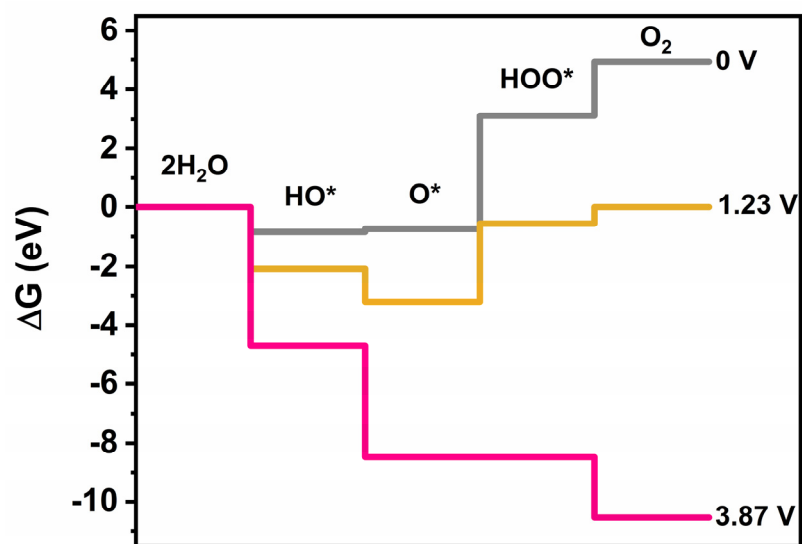


Figure S28. Free energy profiles for the OER over bare NiFe alloy at zero potential ($U=0$), equilibrium potential for oxygen evolution ($U=1.23$ V), and minimal potential where all steps become downhill.

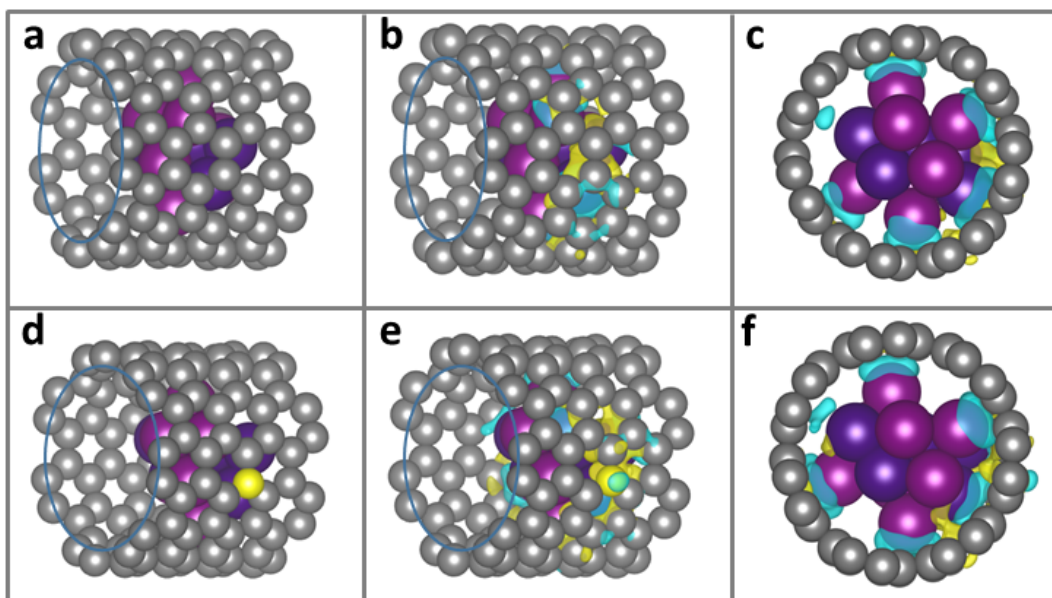


Figure S29. Structures of a) pure CNT encapsulated NiFe alloy and d) N-doped CNT encapsulated NiFe alloy. Charge density difference maps of different models: b) side view and c) front view of pure CNT encapsulated NiFe alloy, and e) side view and f) front view of N-doped CNT encapsulated NiFe alloy (gray, yellow, purple and deep purple spheres are corresponding to C, N, Ni, and Fe atoms, respectively). The yellow and blue areas represent electron accumulation and depletion with the same isosurface value of 0.002 electrons/ \AA^3 , respectively.

Table S10. Elemental analysis data for NiFe-N-CNT samples prepared at different temperatures (batches were measured in triplicate).

	Mass /mg	Carbon %	Hydrogen %	Nitrogen %
NiFe-N-CNT-600°C	1.67	39.74	0.30	14.59
NiFe-N-CNT-600°C	1.61	39.53	0.29	15.04
NiFe-N-CNT-600°C	1.60	39.60	0.31	15.11
NiFe-N-CNT-700°C	1.65	45.86	0.08	4.16
NiFe-N-CNT-700°C	1.51	45.34	0.10	4.47
NiFe-N-CNT-700°C	1.53	45.52	0.11	4.40
NiFe-N-CNT-800°C	1.64	40.87	0.06	2.15
NiFe-N-CNT-800°C	1.67	41.23	0.05	2.05
NiFe-N-CNT-800°C	1.62	40.28	0.03	2.03
NiFe-N-CNT-900°C	1.49	42.63	0.04	1.80
NiFe-N-CNT-900°C	1.43	43.43	0.04	1.82
NiFe-N-CNT-900°C	1.70	43.30	0.03	1.85
NiFe-N-CNT-1000°C	1.50	41.10	0.02	1.13
NiFe-N-CNT-1000°C	1.65	41.51	0.02	1.21
NiFe-N-CNT-1000°C	1.39	40.98	0.02	1.15
NiFe-N-CNT-1100°C	1.45	37.96	0.01	0.53
NiFe-N-CNT-1100°C	1.50	37.40	0.02	0.55
NiFe-N-CNT-1100°C	1.44	37.10	0.02	0.58

Table S11. Summary of catalysts in the present study vs. selected representative noble metal-free catalysts in the literature (catalysts loaded on glassy carbon electrodes).

Catalysts	Electrolyte	Loading amount (mg/cm ²)	Overpotential for OER at 10 mA/cm ² (vs. RHE)	Overpotential for HER at 10 mA/cm ² (vs. RHE)	Ref.
NiFe-N-CNT-rGO	1M KOH	0.38	270 mV	230 mV (NiFe-N-CNT)	This work
NiFe-CNT	1M KOH	0.2	330 mV	210 mV	8
FeCoNi-graphene	1M KOH	0.32	325 mV	211 mV	4
NiFe-graphene	1M KOH	0.32	280 mV	-	9
Ni ₃ FeN/NRGO hybrid	0.1M KOH	0.1	400 mV	-	10
NiFe/CNx	0.1M KOH	0.5	360 mV	-	11
NiFeOH-N-Graphene	0.1M KOH	0.25	337 mV	-	12
NiFeLDH-graphene	1M KOH	0.283	210 mV	300 mV	13
NiFe LDH	1M KOH	0.16	280 mV	-	14
Carbon encapsulated NiFe	1M KOH	1.02	274 mV	195 mV	15
N-CNT encapsulated NiFe	1M KOH	0.5	274 mV	202 mV	16

References

1. Z. Xu, H. Sun, X. Zhao and C. Gao, *Adv. Mater.*, 2013, **25**, 188.
2. B. Ravel and M. Newville, *J. Synchrotron Rad.*, 2005, **12**, 537.
3. A. L. Ankudinov, B. Ravel, J. J. Rehr and S. D. Conradson, *Phys. Rev. B*, 1998, **58**, 7565.
4. Y. Yang, Z. Lin, S. Gao, J. Su, Z. Lun, G. Xia, J. Chen, R. Zhang and Q. Chen, *ACS Catal.*, 2016, **7**, 469.
5. J. Su, Y. Yang, G. Xia, J. Chen, P. Jiang and Q. Chen, *Nat. Commun.*, 2017, **8**, 14969.
6. L.-L. Feng, G. Yu, Y. Wu, G.-D. Li, H. Li, Y. Sun, T. Asefa, W. Chen and X. Zou, *J. Am. Chem. Soc.*, 2015, **137**, 14023.
7. Á. Valdés, Z.-W. Qu, G.-J. Kroes, J. Rossmeisl and J. K. Nørskov, *J. Phys. Chem. C*, 2008, **112**, 9872.
8. X. Zhang, H. Xu, X. Li, Y. Li, T. Yang and Y. Liang, *ACS Catal.*, 2016, **6**, 580.
9. X. Cui, P. Ren, D. Deng, J. Deng and X. Bao, *Energy Environ. Sci.*, 2016, **9**, 123.
10. Y. Fan, S. Ida, A. Staykov, T. Akbay, H. Hagiwara, J. Matsuda, K. Kaneko and T. Ishihara, *Small*, 2017, **13**, 1700099.
11. S. Ci, S. Mao, Y. Hou, S. Cui, H. Kim, R. Ren, Z. Wen and J. Chen, *J. Mater. Chem. A*, 2015, **3**, 7986.
12. C. Tang, H.-S. Wang, H.-F. Wang, Q. Zhang, G.-L. Tian, J.-Q. Nie and F. Wei, *Adv. Mater.*, 2015, **27**, 4516.
13. S. Yin, W. Tu, Y. Sheng, Y. Du, M. Kraft, A. Borgna and R. Xu, *Adv. Mater.*, 2018, **30**, 1705106.
14. Le Yu, J. F. Yang, B. Y. Guan, Y. Lu and X. W. D. Lou, *Angew. Chem. Int. Ed.*, 2018, **130**, 178.
15. S.-W. Park, I. Kim, S.-I. Oh, J.-C. Kim and D.-W. Kim, *J. Catal.*, 2018, **366**, 266.
16. X. Zhao, P. Pachfule, S. Li, J. R. J. Simke, J. Schmidt and A. Thomas, *Angew. Chem. Int. Ed.*, 2018, **57**, 8921.